Journal of Materials Chemistry A

ROYAL SOCIETY OF CHEMISTRY

PAPER

View Article Online
View Journal | View Issue

Cite this: J. Mater. Chem. A, 2026, 14, 22533

Probing electrochemical phenomena in commercial pouch cells using a multimodal magnetic resonance approach

Konstantin Romanenko *[a] and Nikolai I. Avdievich[b]

Received 15th March 2026
Accepted 14th April 2026

DOI: 10.1039/d6ta02247b

rsc.li/materials-a

Further advances in portable electrochemical energy storage will increasingly depend on multifunctional *in situ* diagnostic tools capable of probing materials at the molecular level under realistic operating conditions. This capability is essential for achieving an optimal balance between energy density, cycle life, and safety. The increasing energy density of battery cells reinforces the need for rapid, reliable, and non-destructive diagnostics, including evaluation of state-of-health (SoH) and state-of-charge (SoC). Nuclear magnetic resonance (NMR) spectroscopy and imaging (MRI) are highly sensitive to the environment and dynamics of key electrochemical elements, but most common industrial cell designs present significant obstacles: (a) interrogated nuclear spins are shielded from the radio-frequency (RF) field by conductive metallic structures such as casings and jelly roll sheets of the current collectors, and (b) magnetism from bulk metallic components causes misregistration artefacts and reduces resolution and signal-to-noise ratio. Surface-scan MRI and plug-and-play (PnP) NMR are two distinct *in situ* modalities designed to address these challenges. In this work, we combine the PnP RF adapter and surface-scan MRI sensor into a single multimodal device suitable for a wide range of academic and industrial applications, including SoH analysis and recycling. We illustrate the capabilities of this approach through complementary NMR and MRI experiments, highlighting diverse lithium environments and their transformations during electrochemical cycling in commercial $LiCoO_2$||graphite pouch cells.

1 Introduction

Traditional electrochemical techniques, such as galvanostatic cycling, cyclic voltammetry (CV), and electrochemical impedance spectroscopy (EIS), rely on several integral indicators, such as voltage, capacity, impedance, and their derivatives. These commonly used methods lack molecular-level detail and spatial resolution, often leading to inconclusive or inconsistent results when investigating complex multiphase, interfacial electrochemical phenomena and subtle degradation or mechanical defects. To gain deeper insight into electrochemical systems, the academic community has explored a suite of advanced *in situ* and *operando* characterization techniques,[1–8] including X-ray diffraction (XRD), Fourier-transform infrared spectroscopy (FT-IR), atomic force microscopy (AFM), Auger electron spectroscopy (AES), computed tomography (CT), ultrasonic wave imaging, magnetometry, and magnetic resonance (MR) methods such as nuclear magnetic resonance (NMR) spectroscopy and magnetic resonance imaging (MRI). Among these, state-of-the-art MR techniques stand out for their exceptional sensitivity to electrochemical phenomena and material properties, including structure, morphology, magnetism, ionic transport, and molecular-scale dynamics.[8–45]

Unlike diffraction-based approaches, which primarily detect heavier atomic species, MR techniques excel in probing nuclei throughout the periodic table, provided they have a non-zero spin. This makes MR particularly relevant for battery research, as many key electrochemical elements in electrodes and electrolytes possess NMR-active isotopes, including ^{7}Li, ^{23}Na, ^{1}H, ^{19}F, ^{31}P, ^{55}Mn, and ^{59}Co. The battery industry has prioritized Li- and Na-ion-based electrochemical systems, and these, along with other chemical elements, represent some of the most sensitive NMR probe species. MR experiments span a wide range of contrast mechanisms operating across multiple length and time scales, enabling discrimination of signals based on molecular structure, dynamics, and magnetic properties.

A long-standing obstacle in applying NMR to commercial battery cells has been the attenuation of radio-frequency (RF) signals by metal casings and tightly wound 'jelly roll' current-collector foils. Such architectures are some of the most energy-efficient designs, widely adopted in pouch, prismatic, and cylindrical cells. These conductive elements act as effective RF shields, preventing the excitation RF field (B_1) from penetrating the interior of the cell, where the nuclei of interest reside. As a result, NMR signal detection becomes effectively impossible. This limitation has largely restricted the state-of-

[a]Université Paris-Saclay, CEA, CNRS, NIMBE, Gif-sur-Yvette, 91191, France. E-mail: konstantin.romanenko@cea.fr
[b]Max-Planck Institute for Biological Cybernetics, Tübingen, 72076, Germany

the-art electrochemical NMR to flat parallel-electrode configurations in 'coin' or Swagelok-type cells not fully encased in conductive materials.[7–29,31–35] Sufficient RF penetration can be achieved *via* the skimming mechanism by aligning the electrodes with the direction of the B_1 field. Although the simplicity of such model cells is key to informative *in situ* NMR experiments, optimistic outcomes of such tests often do not translate directly to practical battery prototypes.

In commercial cells, non-uniform spatial distributions of current density and SoC arise from factors such as the large area of current collectors, tab positioning, and finite electrode thickness. This introduces ionic concentration gradients and associated kinetic phenomena that occur in electrodes of resting and operating batteries.[44,46–53] Solid-state diffusion, phase transitions, SEI formation, and metal plating can modulate battery performance. These processes lead to density gradients, volumetric deformation, particle fracturing, increased impedance or loss of electrical contact, and accelerated capacity fade.[54–58]

A further methodological challenge arises from the magnetism of battery terminals, extended tabs, steel casings, and paramagnetic electrode[59–61] materials. These elements generate strong local magnetic-field gradients ($\sim$100 s G cm^{-1})[39] that affect the quality of MR experiments.[62–64]

The first notable *in situ* MR studies of commercial battery prototypes emerged around 2019.[38–41,43–45] The challenges described above can now be largely addressed using plug-and-play (PnP) NMR[30] and surface-scan MRI[41–45] methods, two conceptually independent analytical approaches. The former technique[30] provides a quantitative description of the chemical environments of electrochemically active elements (*e.g.*, Li, Na, Co, *etc.*) in conventional NMR terms. The current collectors of the cell (*e.g.*, aluminum and copper sheets of the cathode and anode, respectively) form a distributed conductive structure whose frequency-dependent impedance at NMR frequencies enables capacitive RF coupling and a high-fill-factor resonant detection volume. The active electromaterials confined between the current collectors serve as an NMR sample. Ion intercalation and transfer between cathode and anode can be directly observed, along with metal plating, electrolyte degradation, and solid–electrolyte interphase (SEI) formation. In addition, NMR lineshapes exhibit anisotropic properties due to bulk magnetic susceptibility (BMS) effects associated with paramagnetic electrode coatings.[14,15,30]

Surface-scan MRI[41] represents an optimal inside-out MRI[38] approach, employing rapid, distortion-free imaging protocols.[39–41] A recent advancement yielding dramatic gains in sensitivity has been achieved through the development of unilateral RF sensors based on a parallel-plate architecture combined with solid-state detection media.[45] By mapping magnetic field (B_0) perturbations near the cell surface using purely phase-encoded two-dimensional (2D) *k*-space sampling, surface-scan MRI enables interrogation of magnetic susceptibility and current-density distributions within the cell. This principle allows the detection of various defect types as well as solid-state processes in electrodes, such as magnetic phase transitions, ion transport, and metal plating.[41–45]

In this work, we combine the surface-scan MRI sensor[45] and PnP NMR adapter[30] in a single multimodal device. Such a composite probe enables a wide range of experimental protocols to be efficiently executed across battery states (SoH, SoC) and operating modes, without repetitive or time-consuming hardware manipulations and associated standard procedures (*e.g.*, shimming, temperature equilibration). Importantly, the coherent acquisition of complementary *in situ* NMR and MRI metrics unlocks their predictive potential.

2 Results and discussion

2.1 Multimodal probe architectures

Fig. 1 presents a schematic of the multimodal MR probe, which integrates surface-scan MRI (blue) and PnP NMR (black) RF sub-

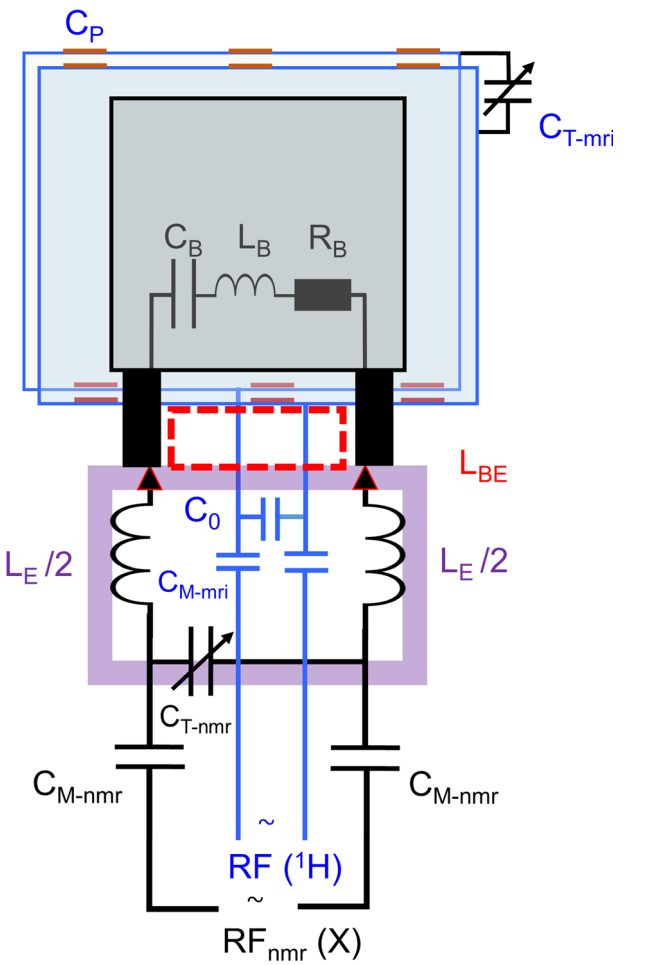

Fig. 1 Electronic schematic of the multimodal RF probe comprising PnP NMR (black) and surface-scan MRI (blue) RF subcircuits. The PnP NMR circuit includes a variable tuning capacitor ($C_{T\text{-}nmr}$), matching capacitors ($C_{M\text{-}nmr}$; balanced configuration), the adapter inductive loop (L_E), and the reactive and resistive elements of the battery cell (C_B, L_B, L_{BE}, R_B). The battery tabs are connected to the NMR circuit at terminals marked by black triangles. The surface-scan MRI circuit consists of distributed capacitors (C_P) and tuning ($C_{T\text{-}mri}$) and matching ($C_{M\text{-}mri}$) capacitors. The battery cell (grey) is positioned in contact with the working surface of the MRI sensor (blue rectangle).

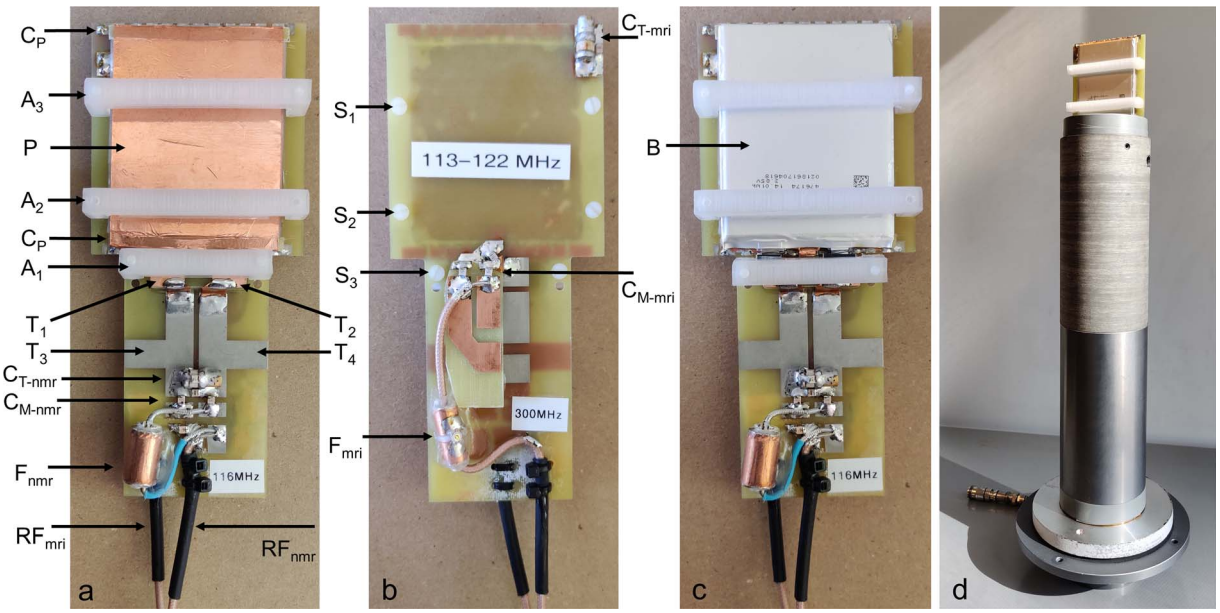

Fig. 2 Photographs of the front (a) and back (b) sides of the multimodal RF probe. Visible components include the working surface (P) of the parallel-plate resonator (~50 μm copper foil with a 1 mm silicone detection medium); variable tuning ($C_{T\text{-mri}}$) and fixed matching ($C_{M\text{-mri}}$) capacitors; fixed ceramic capacitors (C_P) located between copper sheets above and below the silicone layer; terminals of the PnP adapter ($T_{1,2}$) and of the electrochemical cycling circuit ($T_{3,4}$); variable tuning ($C_{T\text{-nmr}}$ and fixed matching ($C_{M\text{-nmr}}$) capacitors of the PnP NMR circuit; shielded cable traps[65,66] (F_{nmr}, F_{mri}) resonant at the X- and ^{1}H frequencies; and 50 Ω coaxial cables (RF_{mri}, RF_{nmr}). (c) A pouch cell – OnePlus7 (b) placed on the resonator's working surface (P) with its tabs connected to the PnP nmr terminals ($T_{1,2}$). The cell is secured by plastic bars A_1–A_3 and screws S_1–S_3; A_1 ensures firm metal-to-metal contact between the battery tabs and the terminals. (d) The multimodal probe with the mounted battery cell installed on the composite probe body compatible with a 7 T vertical-bore magnet (89 mm i.d.).

circuits. The two sub-circuits, operating at the Larmor frequencies of the proton and an X nucleus, respectively, are positioned on opposite sides of a printed circuit board. Photographs of a multimodal probe prototype compatible with a 7 T vertical magnet with an 89 mm bore illustrate the detailed arrangement of the RF components and the battery cell (Fig. 2).

The MRI sub-circuit consists of a parallel-plate resonator, tuning capacitors (C_P, $C_{T\text{-mri}}$), and a matching capacitor ($C_{M\text{-mri}}$). The homogeneity and magnitude of the B_1 field are controlled by the distribution of the capacitors (C_P) along the top and bottom edges of the parallel plates.[45] The resonator volume contains a 1 mm thick silicone layer, which provides the ^{1}H signal used for magnetic field mapping.

The NMR sub-circuit consists of a tuning capacitor ($C_{T\text{-nmr}}$), two matching capacitors ($C_{M\text{-mri}}$), the reactive and resistive elements of the battery cell (C_B, L_B, R_B), and the loop inductance (L_E), which is part of the PnP NMR adapter (Fig. 1). The resonance frequency, ν_0, of the NMR sub-circuit is:

$$\nu_0 = (2\pi)^{-1} (L \cdot C)^{-0.5} \quad (1)$$

Determined by the total capacitance C:

$$C = C_B\, C_{T\text{-nmr}}\, (C_B + C_{T\text{-nmr}})^{-1} \quad (2)$$

And inductance L:

$$L = L_E + L_B \quad (3)$$

The resonance frequency can be controlled by adjusting $C_{T\text{-nmr}}$ and L_E. Note that

$$L_B = L_{BE} + L_{BI} \quad (4)$$

where L_{BI} is the internal inductance of the cell, and L_{BE} is the component of the cell's inductance associated with the loop indicated by the red rectangle (Fig. 1). L_{BE} is largely determined by the interface between battery tabs and the terminals of the PnP NMR adapter. The capacitance of commercial cells exceeds several nF. Thus, in high-field applications, the following conditions apply:

$$C_{T\text{-nmr}} << C_B \quad (5a)$$

and

$$C \approx C_{T\text{-nmr}} \quad (5b)$$

Conditions (5a) and (5b) ensure that the PnP NMR sub-circuit does not require any adjustments specific to different battery cells. In low-frequency applications (*i.e.*, low-γ or low-B_0 experiments), the L_E value (proportional to the loop area) can be increased to satisfy these conditions. Finally, to cancel a common mode produced on the outer surface of the cable shield, two double-tuned cable traps[65,66] were introduced at all inputs of the probe, see Fig. 2.

Based on the same principle, the PnP adapter can be designed as a multi-frequency probe, either as a standalone tool

or as part of the multimodal probe, enabling multi-dimensional NMR experiments and facilitating the analysis of complex NMR lineshapes. The selection of Larmor frequencies depends on the specific chemistries of the cathode, anode, and electrolyte. Materials used in commercial battery cells may contain combinations of the following NMR-active isotopes: ^{6,7}Li, ^{23}Na, ^{31}P, ^{59}Co, ^{55}Mn, ^{51}V, ^{63,65}Cu, ^{27}Al, ^{19}F and ^{1}H. For studies involving low-sensitivity isotopes (*e.g.*, ^{6}Li, ^{17}O, ^{2}H, and ^{13}C), isotopic enrichment of electrode and electrolyte materials can be considered.

Fig. 3 shows a principal electronic schematic of a two-frequency PnP NMR circuit, provided with tuning and matching capacitors ($C_T^{1,2}$ $C_M^{1,2}$) and an LC trap. The concept of double-tuning the NMR probe, achieved by introducing an LC trap in series with the resonance loop, was first proposed by Schnall *et al.*[67] To eliminate cross-talk between (*i.e.*, decouple) the ^{1}H- and X-terminals of the probe, additional band-stop filters (LC(X) and LC(^{1}H), respectively) were introduced into the ^{1}H- and X–RF lines. In this study, we used a multimodal probe (^{7}Li NMR–^{1}H MRI) to analyze the cell under normal conditions (0 < SoC < 100%) and overcharge conditions (100 < SoC < 142%), the latter of which leads to metal plating. A prototype two-frequency PnP ^{7}Li–^{6}Li NMR adapter was designed and experimentally validated.

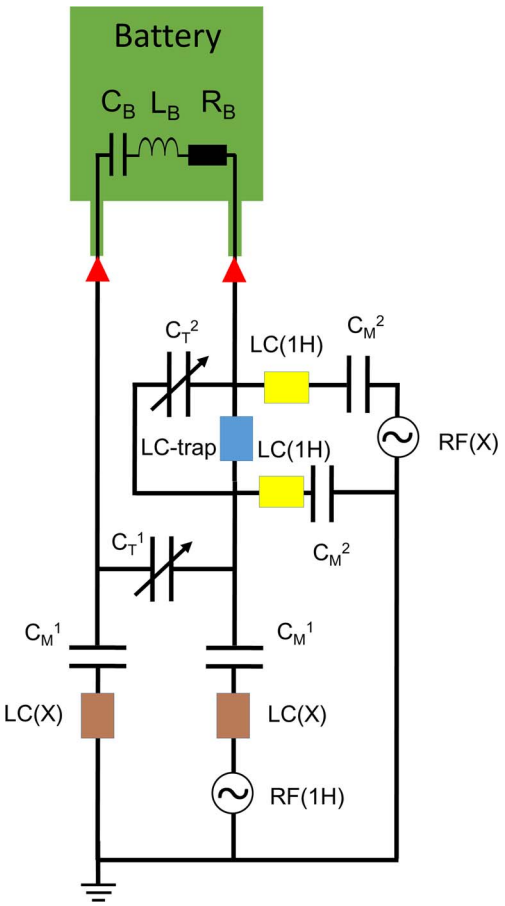

Fig. 3 Principal electronic schematic of a two-frequency PnP RF adapter, including tuning and matching capacitors for each subcircuit ($C_T^{1,2}$, $C_M^{1,2}$), an LC trap (blue rectangle), and band-stop filters (yellow and brown rectangles).

2.2 Plug-and-play NMR

In our previous work, PnP ^{7}Li NMR spectra of commercial pouch cells, based on the $LiCoO_2$ (LCO) cathode and graphite anode, revealed complex lineshapes reminiscent of a first-order quadrupolar triplet at $x \approx 0.5$ (SoC, 100%).[30] Indeed, in model cells, different stages of graphite lithiation manifested as superimposed ^{7}Li NMR triplets.[16–18] In the commercial cells used in this work (OnePlus7 model), quadrupolar multiplets arising from lithiated graphite (Li_xC_6) overlap with the broad ^{7}Li NMR signals originating from the cathode. The analysis of such data can be simplified using a two-frequency (^{7}Li, ^{6}Li) PnP NMR adapter (Fig. 3). For demonstration purposes, one battery cell was overcharged to plate a detectable amount of Li metal on the anode. An overcharge of 1.6 Ah (ΔSoC $\approx$ 43%) was applied at a rate of 0.25C. ^{6}Li and ^{7}Li NMR spectra of this cell are shown in Fig. 4. The Li-metal signal is present in both spectra and can serve as an internal NMR reference (at *ca.* 269 ppm). A triplet-like spectral envelope is apparent in the ^{7}Li NMR data, with the central transition at *ca.* 40 ppm and an apparent quadrupolar splitting of *ca.* 20.5 kHz. The ^{6}Li NMR line at *ca.* 40 ppm

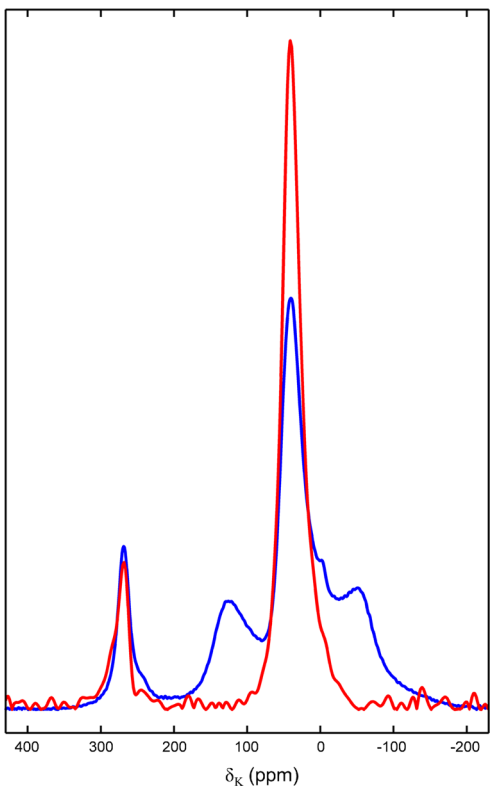

Fig. 4 PnP ^{7}Li (blue) and ^{6}Li (red) NMR spectra of an overcharged pouch cell. For both isotopes, metallic lithium plating produces a narrow resonance at approximately 269 ppm. In contrast, only ^{7}Li nuclei intercalated in Li_xC_6 exhibit detectable quadrupolar splitting.

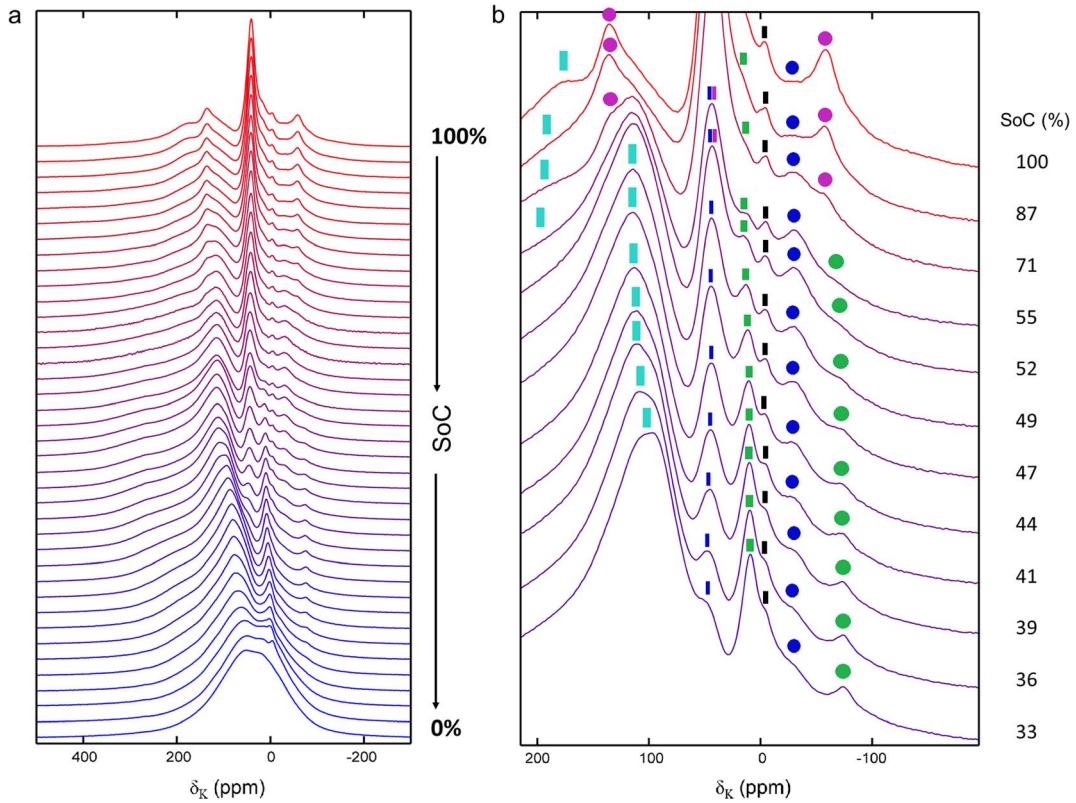

Fig. 5 (a) PnP ^{7}Li NMR spectra of a pouch cell measured at SoC values from 0% to 100%. (b) Approximate positions of the ^{7}Li NMR resonances arising from the anode (Li_xC_6), cathode (LCO), and electrolyte. The central and quadrupolar transitions of Li_xC_6 are highlighted by rectangles and circles, respectively, corresponding to phase 1 (magenta), phase 2 (blue), and phase 2L (green). Apparent LCO resonances are marked with cyan rectangles, while black rectangles indicate the electrolyte peaks.

appears effectively as a singlet due to its small quadrupolar constant.

In situ ^{7}Li NMR spectra of the OnePlus7 cell are shown in Fig. 5a as a 1D stack for a series of SoC values. The initially fully charged cell was discharged in increments of 2.5% SoC. Although an accurate decomposition of static NMR spectra can be challenging, the positions of relatively narrow anode (Li_xC_6) signals can be identified, along with several broad components of the cathode in the low-field region (Fig. 5b).

The lineshape decomposition algorithm developed in this work (Section S1, SI) relies on well-resolved components of the quadrupolar triplets corresponding to stages 1 (LiC_6), 2 (LiC_{12}), and 2L (LiC_{18}) of lithiated graphite (Fig. 5).[16–18,68,69] A low-field shoulder that emerges upon discharging is attributed to

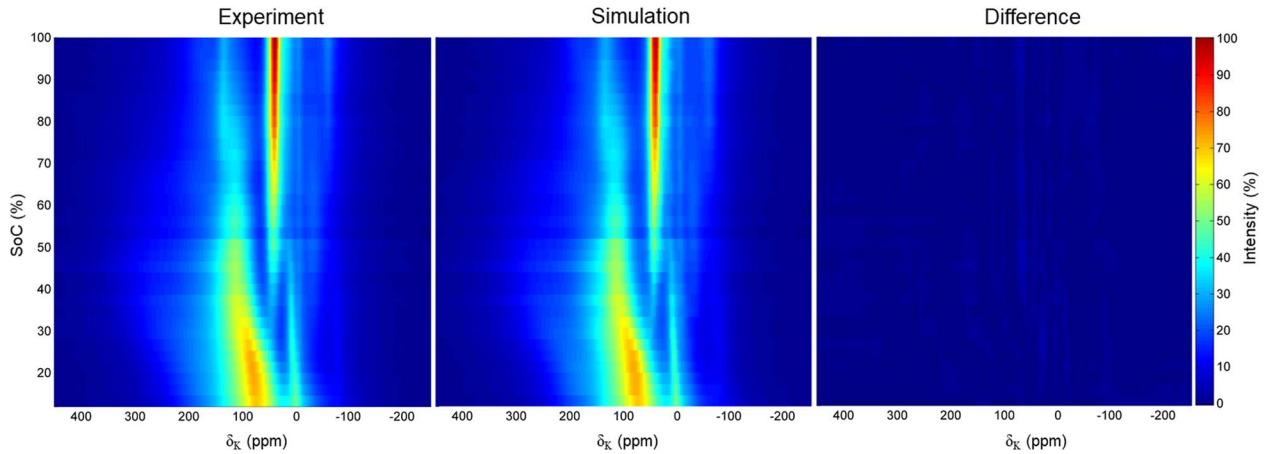

Fig. 6 Experimental (left) and simulated (middle) PnP ^{7}Li NMR spectra of the OnePlus7 pouch cell at SoC values ranging from 12% to 100%. The difference spectrum (experimental minus simulated) is shown on the right.

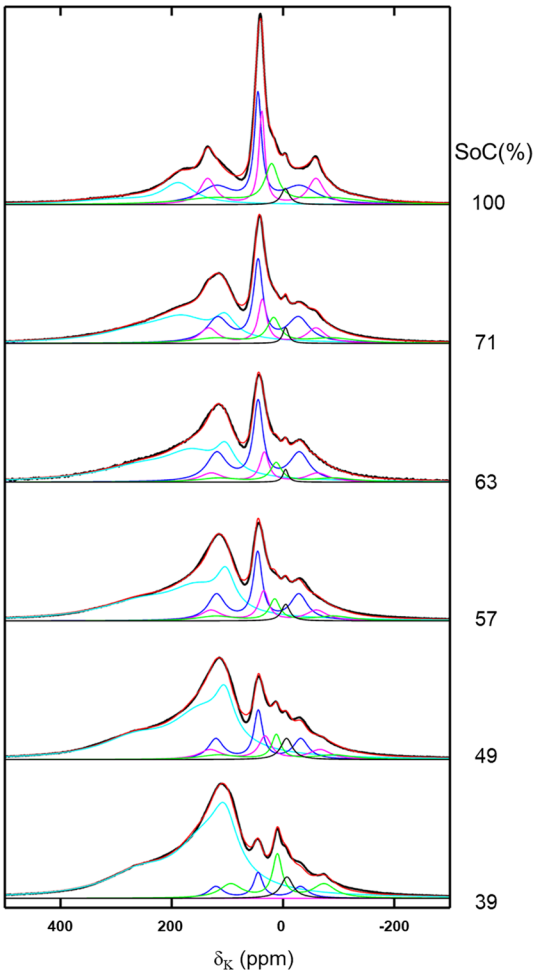

Fig. 7 PnP ^{7}Li NMR lineshape decomposition analysis. Experimental spectrum (black) and simulated lineshape (red). Quadrupolar triplets associated with the Li_xC_6 phases are shown for phase 1 (magenta), phase 2 (blue), and phase 2L (green). The cathode contribution is modeled as a superposition of three lorentzian lines (cyan).

lithiation of the LCO cathode. At SoC > 10%, the cathode contribution to the spectra can be reliably approximated by a superposition of three Lorentzian lines. These Li environments likely reflect variations in the structural and magnetic properties of the Li_xCoO_2 coating[21,70] at both intra- and intergrain levels. Below 20% SoC, the cathode and residual anode resonances begin to merge into a featureless signal. A comparison between experimental and simulated NMR spectra is shown in Fig. 6. Examples of the lineshape decomposition analysis are presented in Fig. 7.

^{7}Li NMR parameters, such as integrated signal intensities (A_i), Knight (δ_K) and chemical (δ) shifts, linewidths ($\Delta\nu_{1/2}$), and first-order quadrupolar splitting (ν_Q), are sensitive to structural and magnetic phase transformations, as well as to morphological changes in electrode materials (Fig. 8).

Integrated intensities (A_i) of ^{7}Li NMR lines associated with the cathode (Fig. 8a) and anode (Fig. 8b) are the most relevant metrics for SoC quantification, as they provide intercalant concentrations in both electrodes. NMR measurements reveal that the lithium content in each electrode changes systematically by approximately one order of magnitude across the SoC range from 10% to 100%. In contrast, electrochemical cycling data frequently display "flat" voltage regions, in which voltage-based SoC estimation becomes unreliable.

Knight shifts and linewidths constitute another set of sensitive metrics for SoC and SoH. In the cathode, δ_K values span an approximately 100 ppm range for each component (Fig. 8c), whereas the corresponding inverse linewidths ($\Delta\nu_{1/2}{}^{-1} \approx T_2^*$) range from 100 to 450 μs (Fig. 8d).

Quadrupolar ^{7}Li NMR lineshapes of Li_xC_6 provide unique insights into anode structure and function. The SoC can be inferred from the relative contributions of each triplet. Our data reveal that three distinct Li_xC_6 environments (1, 2, and 2L) coexist over the SoC range of approximately 50–100%. These observations are likely a consequence of the size distribution of graphite crystallites, leading to heterogeneous electrochemical behavior.

The populations of the Li_xC_6 phases and their individual NMR parameters (δ_K, $\Delta\nu_{1/2}{}^{-1}$ of central and quadrupolar transitions, and ν_Q) vary with SoC in a complex manner, see Fig. 8e–h. At SoC < *ca.* 45%, a systematic decrease in δ_K may signal the emergence of 3L (LiC_{27}) mixed with other low-density phases 4L (LiC_{36}) and 1′. This interpretation is further supported by abrupt changes in ν_Q and $\Delta\nu_{1/2}$ of both the central and quadrupolar transitions. Accurate identification of low-density phases from *in situ* ^{7}Li NMR data remains challenging due to their low concentrations. A relatively narrow signal from the electrolyte ($LiPF_6$) is detectable at SoC > 10%. Its chemical shift is influenced by the SoC-dependent magnetic susceptibility of the cell, making it a sensitive metric for assessing SoC in the 10–50% range (Fig. 8i).

Following the Li metal plating process with PnP ^{7}Li NMR reveals resonance lines within a characteristic Knight shift range (245–270 ppm; Fig. 9a). The main line at 270 ppm and a high-field shoulder at *ca.* 248 ppm emerge at SoC > 110% and gradually increase with the level of overcharge. The Knight shift can vary[14] depending on the metallic cluster morphology, orientation, and conductivity influenced by the interface chemistry. The integrated area of these signals as a function of SoC is shown in Fig. 9b. It should be noted that ^{7}Li NMR detects only metallic lithium within the near-surface region defined by the RF skin depth. This NMR signal is modulated by local orientations of the metal faces with respect to the B_1-field direction.[11,31] Starting at a SoC of ~115%, the amount of NMR-visible Li metal increases approximately linearly with SoC. Because RF penetration is limited in metallic Li, this linear growth likely reflects an increase in NMR-accessible surface area of plated Li; thicker deposits beyond the skin depth contribute little to the observed signal.

2.3 Surface-scan MRI

The surface-scan MRI method has demonstrated a unique capacity to investigate intercalation-dependent magnetism, SoC, solid-state phase transitions, and ion transport in electrodes, while also exhibiting high sensitivity to mechanical

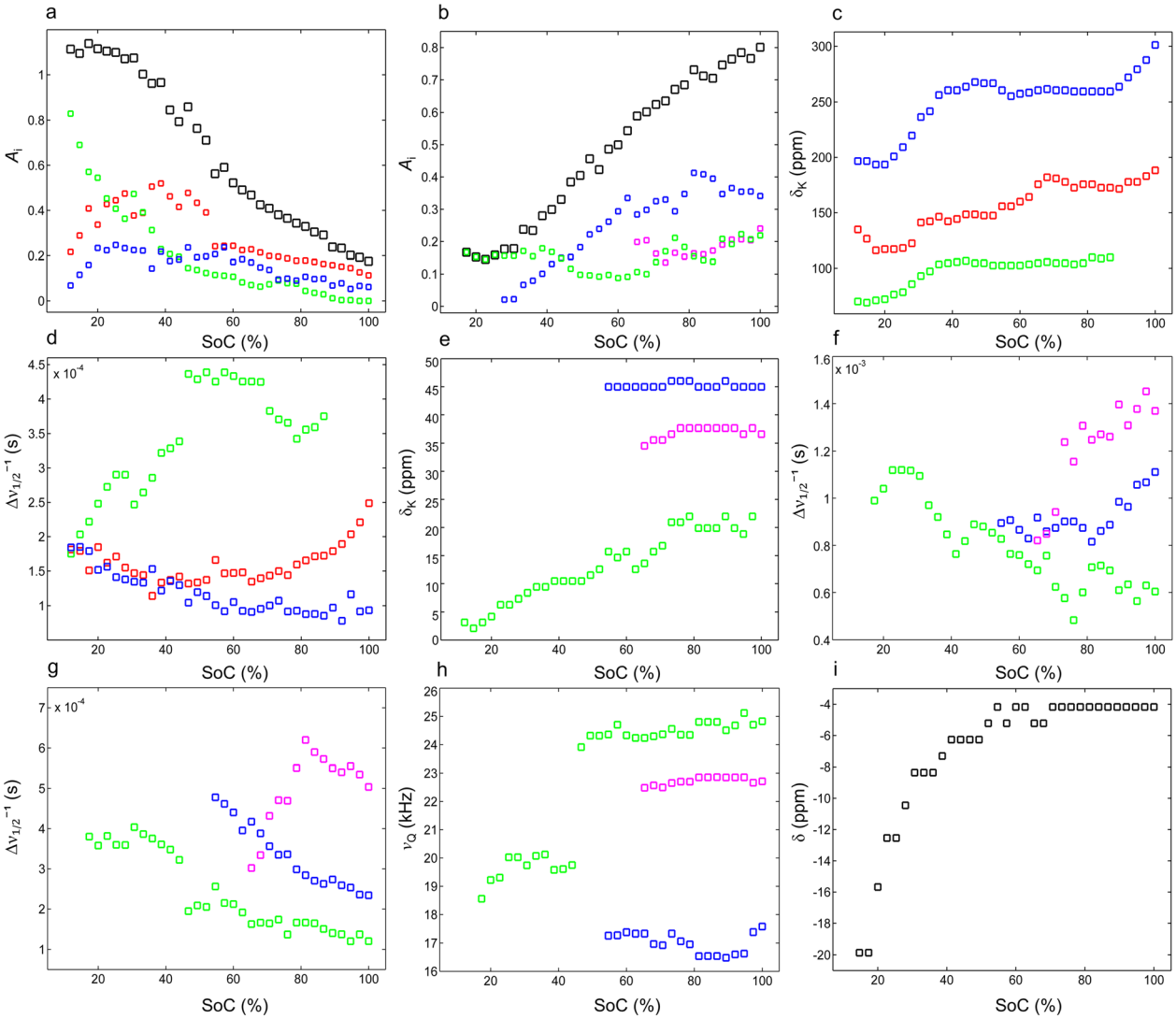

Fig. 8 PnP ^{7}Li NMR parameters of the OnePlus7 pouch cell as a function of SoC from 12% to 100%. (a) Integrated intensities of the composite cathode signal (black) and its low-field (blue), middle (red), and high-field (green) components. (b) Integrated intensities of the composite anode signal (black) and the three quadrupolar triplets associated with Li_xC_6 phase 1 (magenta), phase 2 (blue), and phase 2L (green). (c and d) Knight shifts and inverse linewidths, respectively, of the cathode signals. (e) Knight shifts of the central transitions of Li_xC_6 phase 1 (magenta), phase 2 (blue), and phase 2L (green). (f and g) Inverse linewidths of the central and satellite transitions, respectively, of Li_xC_6 phase 1 (magenta), phase 2 (blue), and phase 2L (green). (h) First-order quadrupolar splittings (ν_q) of Li_xC_6 phase 1 (magenta), phase 2 (blue), and phase 2L (green). (i) ^{7}Li NMR chemical shift of the electrolyte. The uncertainties of measurements are comparable to the marker size.

defects and currents in operating batteries.[40–45] A commercial battery cell (pouch, prismatic, or cylindrical) placed in a uniform polarizing magnetic field (B_0) generates characteristic magnetic-field perturbations (ΔB), enabling the prediction of the magnetic susceptibility distribution within electrode materials:[38,39,44,45]

$$\Delta B \propto \chi(\mathrm{SoC}) \tag{6}$$

To facilitate the analysis of SoC-dependent MRI data (B_{SoC}), magnetic field components that do not vary with SoC should be removed by subtraction of a suitable reference map, ΔB_r:

$$B_{\mathrm{SoC}} = \Delta B(\mathrm{SoC}) - \Delta B_r \tag{7}$$

where, by convention,

$$\Delta B_r = \Delta B(\mathrm{SoC} = 100\%) \tag{8}$$

is the magnetic field map of a 'healthy' fully charged cell in the rest state.

In general, the choice of the reference map, ΔB_r, is context-dependent and should reflect the specific contrast mechanism of interest. For B_{SoC} mapping, the objective is to isolate the magnetic field contribution arising from reversible electrochemical processes while suppressing static or geometry-driven components that are independent of SoC (*e.g.*, dipolar fields from current collectors, tabs, and other metallic elements).

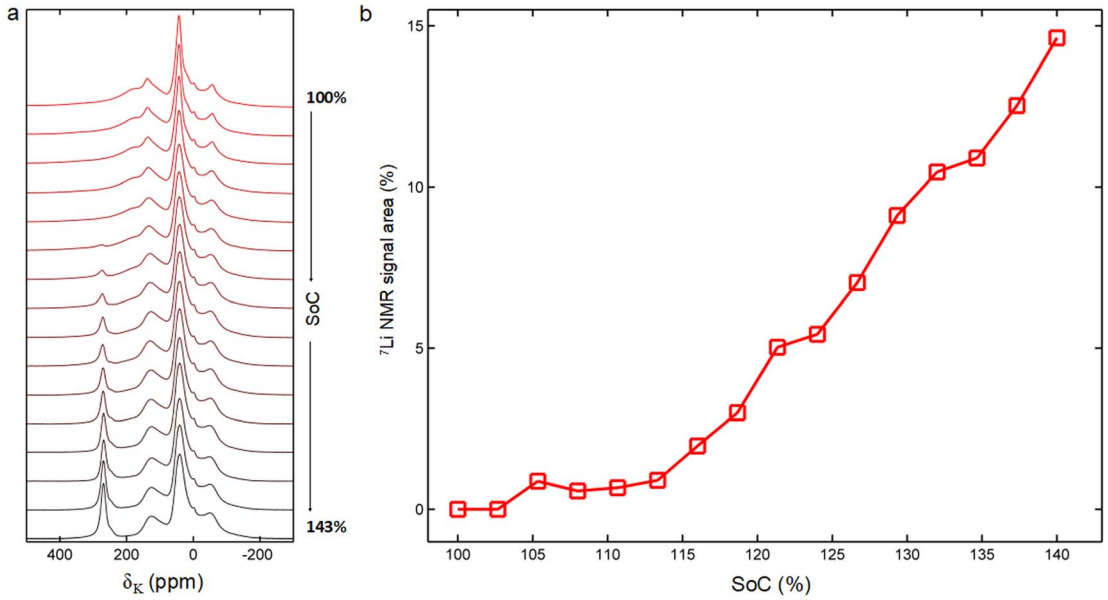

Fig. 9 (a) PnP ^{7}Li NMR spectra of a OnePlus7 pouch cell at different stages of overcharge. (b) Integrated NMR intensities associated with metallic lithium deposition as a function of SoC.

For a given "healthy" battery, ΔB_r is therefore defined as the field map acquired at a well-defined reference state, typically SoC = 100%. All subsequent maps are expressed relative to this baseline, *i.e.*, ΔB(SoC)–ΔB_r, ensuring that the resulting contrast predominantly reflects changes in the active materials. This normalization minimizes contributions from invariant structural features and improves comparability across measurements.

The robustness of this approach relies on the reproducibility of the magnetic field maps. Our MRI methodology is inherently based on spatial pattern recognition: cells of identical design and electrochemical state are expected to produce field maps that are indistinguishable within an experimental uncertainty ε. In this work, repeated surface-scan MRI measurements on the same cell yield ΔB maps reproducible within $\varepsilon \approx 0.2$ ppm, which defines the practical sensitivity limit of the method. This reproducibility enables a quantitative criterion for degradation assessment. Specifically, deviations between reference-state maps acquired at different stages of cycling can be evaluated as:

$$\varepsilon = \Delta B(\text{SoC} = 100\%, \text{cycle } 0) - \Delta B(\text{SoC} = 100\%, \text{cycle N}) \quad (9)$$

If ε remains within the experimental uncertainty ($\varepsilon \leq 0.2$ ppm), the cell can be considered magnetically and structurally stable, indicating negligible degradation. Conversely, systematic deviations beyond this threshold reflect irreversible changes in magnetic susceptibility distributions, which may arise from processes such as material degradation, loss of active lithium, or mechanical deformation.

Finally, differences observed between nominally identical cells at the same SoC can be attributed to variations in manufacturing or assembly (*e.g.*, coating inhomogeneity, electrode misalignment, or tab geometry). This sensitivity to spatial heterogeneity provides a direct basis for non-destructive quality control and defect identification in industrial battery cells.

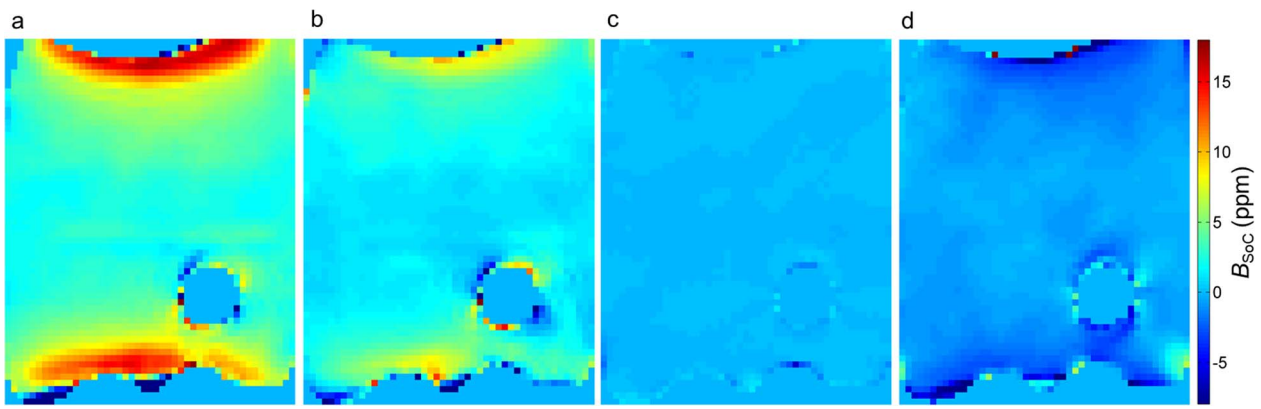

Fig. 10 (a–d) Examples of B_{SoC} maps of a OnePlus7 pouch cell at SoC values of 0%, 10.6%, 100%, and 142.6% (overcharge), respectively.

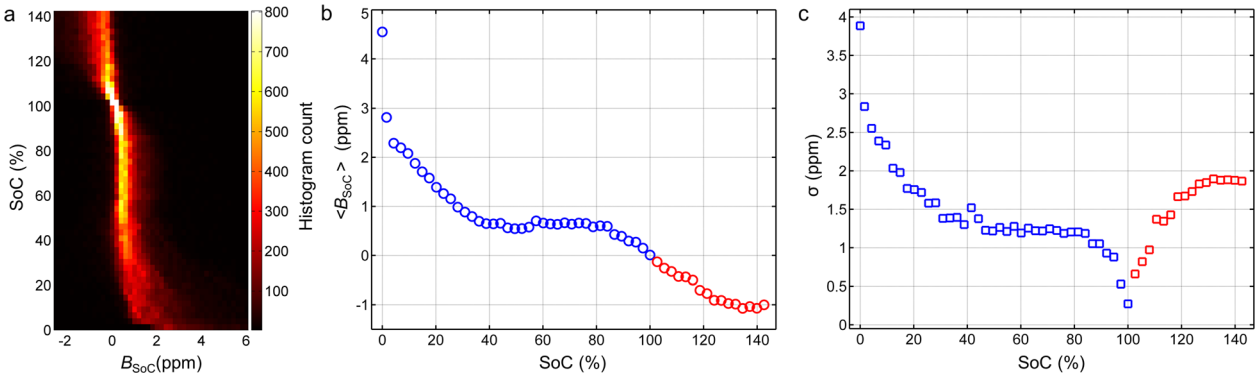

Fig. 11 B_{SoC}-Derived metrics of a OnePlus7 pouch cell for SoC levels between 0% and 143%. (a) Histograms of B_{SoC} distributions. (b) Means, <B_{SoC}>. (c) Standard deviations, σ. The uncertainties of measurements are smaller than the marker size.

Fig. 10 shows four representative examples of B_{SoC} maps of an LCO-based pouch cell (Table S1, SI) at several SoCs (0, 10.6, 100 and 142.6% overcharge). Histograms of B_{SoC} distributions and corresponding means, <B_{SoC}>, and standard deviations, σ, are shown in Fig. 11a, b and c, respectively. Due to the strong magnetic susceptibility contrast between LCO phases O3-R2 ($0.58 < x < 0.75$) and O3-R1 ($0.94 < x < 1$),[59,60] the B_{SoC} data are expected to be particularly informative in the two-phase region $0.75 < x < 0.94$ (12% < SoC < 50%).[44] The statistical analysis of B_{SoC} maps (Fig. 11) is consistent with these expectations and indicates several characteristic SoC regions: (A) 0–5% (O3-R1 dominated); (B) 5–40% (O3-R2 → O3-R1 – transition, mixed phase); (C) 40–82% (O3-R2 dominated); (D) 82–100% (O3-M – dominated); (E) 100–140% (overcharge – metal plating).

The MRI data suggest that <B_{SoC}> and σ can be good metrics of SoC in the intervals 0–40% and 82–130%, Fig. 11b and c. Outside these regions, the parameters plateau, thus leaving a gap (40–82%) in the SoC analysis. Note, these conclusions are specific to characteristic magnetic phases of LCO. PnP NMR, a complementary approach, allows accurate predictions of SoCs within the range from 10 to 100% (Fig. 5, 6 and 8). Thus, combining our *in situ* MRI and NMR data enables accurate analysis of intercalation processes and metal plating in the SoC range from 0 to 140%.

Upon overcharging, the LCO cathode becomes excessively delithiated, which destabilizes both its crystal structure and interfacial chemistry. Progressive delithiation increases the Co^{4+} fraction and associated paramagnetism, leading to enhanced susceptibility variations and NMR line broadening. In terms of MRI experiments, overcharging resulted in a 1 ppm decrease in <B_{SoC}>, indicating an overall increase in paramagnetism of the cathode (Fig. 11b). A 1.5 ppm increase in σ (Fig. 11c) suggests a greater magnetic heterogeneity that can be linked to SoH degradation and correlates with the metal plating observed with PnP NMR.

Note that B_{SoC} maps describe magnetic field patterns that can occur due to spatial variations in (a) concentrations of intercalant ions and oxidation states in the electrode coating; (b) current density resulting from common geometrical constraints in battery designs; (c) properties of electrode coating such as the thickness, impurity content, type and amount of conductive and electrolyte additives, and the quality of electronic contact between active particles and the current collector.

3 Conclusions

This work demonstrates the potential of a highly versatile platform for the assessment of SoC and SoH in state-of-the-art pouch cells. Surface-scan MRI and PnP NMR, integrated within a single multimodal device, enable a broad range of complementary quantitative metrics that cannot be achieved by standalone NMR or MRI techniques. The optimal choice of MR observables inherently depends on cathode and anode chemistries. However, the widespread use of lithium- and sodium-based systems containing highly NMR-sensitive isotopes (^{7}Li and ^{23}Na) makes MR-based analytics broadly applicable.

Within the PnP NMR framework, the current collectors act as an efficient RF probe due to the high fill factor of the dense electrode architecture. PnP NMR preserves the core capabilities of conventional NMR spectroscopy while enabling high-throughput measurements. We demonstrated strong sensitivity of PnP NMR to SoC, carbon anode intercalation chemistry, and, in particular, metal plating. In many cases, cathode analysis is also feasible, although severe paramagnetic line broadening in some materials may require extended protocols based on variable carrier frequency. The PnP NMR experiments enable clear discrimination of graphite staging and identification of multiple lithium environments in the lithium cobalt oxide (LCO) cathode. Notably, the data reveal that in LCO cells, the anode is not fully lithiated at a voltage-defined SoC of 100%, with the LiC_6 phase accounting for only ~30–40% of the graphite. This observation highlights the limitations of conventional voltage-based metrics and demonstrates the added value of NMR methodology.

We note that the key findings of this work are rooted in broadly applicable physical processes. Graphite remains the dominant anode material in Li-ion batteries, and the ability to resolve its lithiation stages (Li_xC_6) is therefore intrinsically general. The PnP NMR approach directly tracks the evolution of these phases during operation, independent of the specific cathode chemistry.

The diverse intercalation-dependent magnetic phase behaviors of layered transition metal oxides and polyanion systems

are critical for achieving strong surface-scan MRI contrast. Surface-scan MRI complements PnP NMR by circumventing linewidth limitations and providing spatially resolved maps of magnetic field perturbations. This enables non-invasive visualization of SoC heterogeneity and magnetic phase transitions within intact industrial cells. Beyond the susceptibility-based imaging, *operando* surface-scan MRI can also detect metal plating through analysis of current density distributions. Although more complex to implement, these measurements further extend the scope of the multimodal approach.

From the MRI perspective, LCO represents a demanding and informative test system. Its continuous and multi-phase magnetic susceptibility evolution across lithiation states provides a stringent benchmark for surface-scan MRI. In contrast, simpler biphasic systems such as lithium iron phosphate (LFP) are expected to produce more straightforward MRI responses. Successful application to LCO therefore supports the broader applicability of the method to a wide range of battery chemistries.

Overall, the multimodal MR approach provides a powerful and scalable platform for fundamental studies and practical battery analysis applications, including quality control, safety diagnostics (*e.g.*, metal plating and mechanical defects), and recycling.

4 Methods

4.1 NMR and MRI experiments

Experiments were performed using a Bruker Avance NEO console and a 7 T vertical-bore magnet (I.D. 154 mm) equipped with a triaxial gradient set (79 G cm^{-1} at 200 A). Multimodal RF probes were constructed from 1.5 mm thick copper-plated PCBs, copper foil, non-magnetic variable capacitors (Johanson, Model 5641; 1.0–30 pF; 250 V, USA), fixed capacitors (Exxelia, 4–27 pF; 500 V), and 50 Ω coaxial cables with BNC connectors. The parallel-plate resonator consisted of a 1 mm thick silicone sheet (65 × 60 mm) sandwiched between two copper foil sheets. Twenty-two capacitors (C_P ∼24 pF each) were evenly distributed along two opposite edges of the resonator (Fig. 2).

PnP ^{7}Li NMR experiments were performed at a carrier frequency of 116.64 MHz using a single-pulse sequence: 5 μs excitation RF pulse, 6.5 μs pre-acquisition delay, spectral width of 500 kHz, 1024 complex data points, and 1 s magnetization recovery delay. The B_1 magnitude estimated from nutation experiments was ∼10 kHz ($\pi/2$ pulse duration ≈ 25 μs) at 1000 W transmitter power. Each spectrum was acquired with 500 signal averages, yielding a total measurement time of ∼9 min. Chemical shifts were referenced to an external 1 M LiCl solution (0 ppm). The battery management system (BMS) circuitry connecting the cell tabs was removed to improve RF transmission through the current collectors. This modification does not alter the intrinsic electrochemical behavior of the cell. Specifically, the capacity and voltage window remain unchanged, as they are determined by the electrode materials and electrolyte chemistry. The rate capability may be marginally influenced by differences in external wiring; however, this does not impact the conclusions drawn in this work. We further note that pouch cells without integrated BMS are widely used in both research and industrial contexts (*e.g.*, bare cells supplied for module integration and laboratory testing). The PnP NMR methodology is therefore directly applicable to a broad class of commercially relevant systems.

Surface-scan MRI experiments employed a 2-dimensional centric-scan SPRITE protocol[41,43–45] implemented in the ParaVision 360 environment. Nonselective, low-flip-angle RF pulses (carrier frequency: 300.356 MHz) were followed by a pre-acquisition phase encoding period $T_P{}^0$ (58 μs) and acquisition of FID data under the SPRITE gradient. Each RF pulse had a duration of 1 μs (flip angle ∼$\pi/18$) at 100 W transmitter power. Gradient switching and stabilization intervals were each 0.5 ms. Eight complex points (32 μs) were acquired at time $T_P{}^k$ after each excitation pulse:

$$T_P{}^k = T_P{}^0 + (k-1)\, SW^{-1},\ k = 1-8 \tag{10}$$

where SW is the sampling bandwidth (250 kHz). A 64 × 64 k-space matrix was constructed from eight centrically ordered Cartesian trajectories, separated by a 2 s magnetization recovery delay. The SPRITE protocol generated eight 2D k-space data sets corresponding to phase-encoding periods of 62–90 μs. The imaging plane was aligned with the working surface of the parallel-plate resonator. Phase images were reconstructed using a chirp Z-transform algorithm[71] to provide identical FOVs. A spatial resolution of 1.2 mm was achieved with a gradient magnitude of 0.11 T m^{-1}. A time series comprising eight phase images (φ_k) was reconstructed from a single SPRITE scan, and the local magnetic field offset was obtained as the slope of a linear regression of the temporal phase evolution:

$$\Delta B(\mathbf{r}) = \gamma^{-1}\, \Delta\varphi(\mathbf{r}, T_P)\, \Delta T_P{}^{-1} \tag{11}$$

where γ is the gyromagnetic ratio of protons. The acquisition time for a surface-scan MRI map is approximately 3.5 minutes, using 8 signal averages to enhance the signal-to-noise ratio. All data processing routines were implemented in MATLAB (R2019b, The MathWorks, Inc.).

4.2 Electrochemical cycling

Electrochemical experiments were conducted using a BTS-4008-5V6A-S1 instrument (NEWARE, Hong Kong, China) at 20 °C. Battery cells (Section S2, SI) were cycled galvanostatically at approximately C/8, within the factory-specified voltage cutoff limits of 2.75–4.4 V for the OnePlus7 cells. Overcharging procedures were conducted outside the NMR magnet in a controlled laboratory environment with appropriate safety measures in place, including operation within an exhaust fume hood and the availability of a fire extinguisher.

Author contributions

K. R. conceived the study, developed the experimental protocols, performed the NMR and MRI experiments, and conducted data analysis. The multimodal probes were developed through

close collaboration between N. A. and K. R. Both authors contributed to the preparation and revision of the manuscript.

Conflicts of interest

There are no conflicts to declare.

Data availability

The data supporting this study are available from the corresponding author upon reasonable request.

Supplementary information (SI): details of the NMR lineshape analysis and specifications of the commercial pouch cells used in this study. See DOI: https://doi.org/10.1039/d6ta02247b.

Acknowledgements

K. R. acknowledges financial support from the Agence Nationale de la Recherche (ANR), Project No. ANR-25-CE50-0032-01. N. A. thanks the Deutsche Forschungsgemeinschaft (DFG) for support under Project No. 568670018.

References

1 A. M. Tripathi, W.-N. Su and B. J. Hwang, *Chem. Soc. Rev.*, 2018, **47**, 736–851.
2 D. Liu, Z. Shadike, R. Lin, K. Qian, H. Li, K. Li, S. Wang, Q. Yu, M. Liu, S. Ganapathy, X. Qin, Q. Yang, M. Wagemaker, F. Kang, X. Yang and B. Li, *Adv. Mater.*, 2019, **31**, 1800933.
3 Y. Tian, C. Lin, H. Li, J. Du and R. Xiong, *Appl. Energy*, 2021, **300**, 117386.
4 S. Lee, S. Park, W. Lee, J. Seok, J. Kim, J. Kim and W. Yoon, *Carbon Energy*, 2024, **6**, 12.
5 Z. Deng, *et al.*, *Joule*, 2020, **4**, 2017–2029.
6 Y. Hu, *et al.*, *Proc. Natl. Acad. Sci. U. S. A.*, 2020, **117**, 10667–10672.
7 C. P. Grey and J. M. Tarascon, *Nat. Mater.*, 2016, **16**, 45–56.
8 O. Pecher, J. Carretero-González, K. J. Griffith and C. P. Grey, *Chem. Mater.*, 2017, **29**, 213–242.
9 X. Liu, Z. Liang, Y. Xiang, M. Lin, Q. Li, Z. Liu, G. Zhong, R. Fu and Y. Yang, *Adv. Mater.*, 2021, **33**, 2105207.
10 A. L. Freytag, A. D. Pauric, S. A. Krachkovskiy and G. R. Goward, *J. Am. Chem. Soc.*, 2019, **141**, 13758–13761.
11 E. G. Sorte, N. A. Banek, M. J. Wagner, T. M. Alam and Y. J. Tong, *Chemelectrochem*, 2018, **5**, 2336–2340.
12 S. Benders, M. Mohammadi, C. A. Klug and A. Jerschow, *Sci. Rep.*, 2020, **10**, 1–11.
13 B. J. Walder, M. S. Conradi, J. J. Borchardt, L. C. Merrill, E. J. Deichmann, T. M. Anderson, T. M. Alam and K. L. Harrison, *Sci. Adv.*, 2021, **7**, eabf048.
14 N. M. Trease, L. Zhou, H. J. Chang, B. Y. Zhu and C. P. Grey, *Solid State Nucl. Magn. Reson.*, 2012, **42**, 62–70.
15 L. Zhou, M. Leskes, A. J. Ilott, N. M. Trease and C. P. Grey, *J. Magn. Reson.*, 2013, **234**, 44–57.
16 M. Letellier, F. Chevallier and M. Morcrette, *Carbon*, 2007, **45**, 1025–1034.
17 F. Chevallier, F. Poli, B. Montigny and M. Letellier, *Carbon*, 2013, **61**, 140–153.
18 S. A. Krachkovskiy, *et al.*, *J. Electrochem. Soc.*, 2020, **167**, 130514.
19 B. Key, *et al.*, *J. Am. Chem. Soc.*, 2009, **131**, 9239–9249.
20 F. Poli, J. S. Kshetrimayum, L. Monconduit and M. Letellier, *Electrochem. Commun.*, 2011, **13**, 1293–1295.
21 K. Shimoda, *Electrochim. Acta*, 2013, **108**, 343–349.
22 M. Menetrier, I. Saadoune, S. Levasseur and C. Delmas, *J. Mater. Chem.*, 1999, **9**, 1135–1140.
23 A. B. Gunnarsdóttir, C. V. Amanchukwu, S. Menkin and C. P. Grey, *J. Am. Chem. Soc.*, 2020, **142**, 20814–20827.
24 K. Märker and C. P. Grey, *J. Am. Chem. Soc.*, 2020, **142**, 17447–17456.
25 M. Liu, S. Ganapathy and M. Wagemaker, *Acc. Chem. Res.*, 2022, **55**, 333–344.
26 D. Columbus, *et al.*, *J. Am. Chem. Soc.*, 2022, **144**, 9836–9844.
27 J. M. Stratford, P. K. Allan, O. Pecher, P. A. Chater and C. P. Grey, *Chem. Commun.*, 2016, **52**, 12430–12433.
28 J. M. Stratford, *et al.*, *J. Am. Chem. Soc.*, 2021, **143**, 14274–14286.
29 K. Gotoh, *Batter. Supercaps*, 2021, **4**, 1267–1278.
30 K. Romanenko, N. Avdievich and E. Foy, *J. Am. Chem. Soc.*, 2024, **146**, 29407–29416.
31 S. Chandrashekar, *et al.*, *Nat. Mater.*, 2012, **11**, 311–315.
32 A. J. Ilott, M. Mohammadi, H. J. Chang, C. P. Grey and A. Jerschow, *Proc. Natl. Acad. Sci. U. S. A.*, 2016, **113**, 10779–10784.
33 P. M. Bayley, N. M. Trease and C. P. Grey, *J. Am. Chem. Soc.*, 2016, **138**, 1955–1961.
34 Y. Xiang, *et al.*, *Nat. Nanotechnol.*, 2020, **15**, 883–890.
35 J. D. Bazak, J. P. Allen, S. A. Krachkovskiy and G. R. Goward, *J. Electrochem. Soc.*, 2020, **167**, 140518.
36 K. Romanenko, M. Forsyth and L. A. O'Dell, *J. Magn. Reson.*, 2014, **248**, 96–104.
37 K. Romanenko, L. Jin, P. Howlett and M. Forsyth, *Chem. Mater.*, 2016, **28**, 2844–2851.
38 A. J. Ilott, M. Mohammadi, C. M. Schauerman, M. J. Ganter and A. Jerschow, *Nat. Commun.*, 2018, **9**, 1–9.
39 K. Romanenko and A. Jerschow, *Proc. Natl. Acad. Sci. U. S. A.*, 2019, **116**, 18783–18789.
40 K. Romanenko, P. W. Kuchel and A. Jerschow, *Chem. Mater.*, 2020, **32**, 2107–2113.
41 K. Romanenko and A. Jerschow, *J. Mater. Chem. A*, 2021, **9**, 21078–21084.
42 K. Romanenko and A. Jerschow, *J. Magn. Reson. Open*, 2022, **10–11**, 100061.
43 K. Romanenko and N. Avdievich, *J. Phys. Chem. C*, 2022, **127**, 85–91.
44 K. Romanenko, *et al.*, *Chem. Mater.*, 2023, **35**, 9789–9798.
45 K. Romanenko and N. Avdievich, *J. Magn. Reson. Open*, 2024, **18**, 100141.
46 A. Fernando, M. Kuipers, G. Angenendt, K.-P. Kairies and M. Dubarry, *Measurement: Energy*, 2024, **3**, 100013.
47 K. P. C. Yao, J. S. Okasinski, K. Kalaga, I. A. Shkrob and D. P. Abraham, *Energy Environ. Sci.*, 2019, **12**, 656–665.

48 Z. Chen, D. L. Danilov, R.-A. Eichel and P. H. L. Notten, *Energy Storage Mater.*, 2022, **48**, 475–486.
49 J. I. G. Dawkins, M. Z. Ghavidel, D. Chhin, I. Beaulieu, M. S. Hossain, R. Feng, J. Mauzeroll and S. B. Schougaard, *Anal. Chem.*, 2020, **92**, 10908–10912.
50 B. Pelletier-Villeneuve, B. Krueger, J. R. Adsetts, M.-C. Ricard and B. Schougaard, *ECS Electrochem.*, 2025, **1**, 1972–1976.
51 G. A. Giffin, *Nat. Commun.*, 2022, **13**, 1–9.
52 D. Takamatsu, A. Yoneyama, Y. Asari and T. Hirano, *J. Am. Chem. Soc.*, 2018, **140**, 1608–1611.
53 B.-G. Chae, S. Y. Park, J. H. Song, E. Lee and W. S. Jeon, *Nat. Commun.*, 2021, **12**, 1–9.
54 S. Zhang, *npj Comput. Mater.*, 2017, **3**, 1–10.
55 F. Pistorio, D. Clerici, F. Mocera and A. Somà, *Energies*, 2022, **15**, 9168.
56 J. S. Edge, S. O'Kane, R. Prosser, N. D. Kirkaldy, A. N. Patel, A. Hales, A. Ghosh, W. Ai, J. Chen and J. Yang, *Phys. Chem. Chem. Phys.*, 2021, **23**, 8200–8221.
57 A. Lundkvist, P.-L. Larsson and E. Olsson, *Powder Technol.*, 2025, **466**, 121417.
58 J. S. Menye and M.-B. Camara, *Energies*, 2025, **18**, 342.
59 J. T. Hertz, *et al.*, *Phys. Rev. B*, 2008, **77**, 075119.
60 T. Motohashi, *et al.*, *Phys. Rev. B*, 2009, **80**, 165114.
61 Y. Mekonnen, A. Sundararajan and A. I. Sarwat, *SoutheastCon 2016*, 2016, 1–6.
62 J. R. Reichenbach, R. Venkatesan, D. A. Yablonskiy, M. R. Thompson, S. Lai and E. M. Haacke, *J. Magn. Reson. Imag.*, 1997, **7**, 266–279.
63 M. J. Graves and D. G. Mitchell, *J. Magn. Reson. Imag.*, 2013, **38**, 269–287.
64 M. A. Bernstein, K. F. King and X. J. Zhou, *Handbook of MRI Pulse Sequences*, Elsevier, Oxford, 2004.
65 J. J. Seeber and A. Menon, *Concepts Magn. Reson. Part B*, 2004, **21B**, 26–31.
66 N. I. Avdievich and H. P. Hetherington, *J. Magn. Reson.*, 2007, **186**, 341–346.
67 M. D. Schnall, V. Harihara Subramanian, J. S. Leigh and B. Chance, *J. Magn. Reson.*, 1985, **65**, 122–129.
68 J. R. Dahn, *Phys. Rev. B*, 1991, **44**, 9170–9177.
69 T. Ohzuku, Y. Iwakoshi and K. Sawai, *J. Electrochem. Soc.*, 1993, **140**, 2490–2498.
70 M. C. Tucker, J. A. Reimer, E. J. Cairns, S. Choi and A. Manthiram, *J. Phys. Chem. B*, 2002, **106**, 3842–3847.
71 M. Halse, J. Rioux, S. Romanzetti, J. Kaffanke, B. MacMillan, I. Mastikhin, N. J. Shah, E. Aubanel and B. J. Balcom, *J. Magn. Reson.*, 2004, **169**, 102–117.